Role of Structural and Electronic Properties of Pt and Pt Alloys on Electrocatalysis of Oxygen Reduction

An *In Situ* XANES and EXAFS Investigation

Sanjeev Mukerjee,* Supramaniam Srinivasan,* and Manuel P. Soriaga

Center for Electrochemical Systems and Hydrogen Research and Department of Chemistry, Texas A&M University, College Station, Texas 77843-3402

James McBreen*

Brookhaven National Laboratory, Material Science Division, Department of Applied Science, Upton, New York 11973

ABSTRACT

The electrocatalysis of the oxygen reduction reaction (ORR) on five binary Pt alloys (PtCr/C, PtMn/C, PtFe/C, PtCo/C, and PtNi/C) supported on high surface area carbon in a proton exchange membrane fuel cell was investigated. All the alloy electrocatalysts exhibited a high degree of crystallinity with the primary phase of the type Pt_3M (LI_2 structure with fcc type lattice) and a secondary phase (only minor contribution from this phase) being of the type PtM (LI_0 structure with tetragonal lattice) as evidenced from x-ray powder diffraction (XRD) analysis. The electrode kinetic studies on the Pt alloys at 95°C and 5 atm pressure showed a two- to threefold increase in the exchange current densities and the current density at 900 mV as well as a decrease in the overvoltage at 10 mA cm^{-2} relative to Pt/C electrocatalyst. The PtCr/C alloy exhibited the best performance. *In situ* EXAFS and XANES analysis at potentials in the double-layer region [0.54 V *vs.* reversible hydrogen electrode (RHE)] revealed (*i*) all the alloys possess higher Pt *d*-band vacancies per atom (with the exception of PtMn/C alloy) relative to Pt/C electrocatalyst and (*ii*) contractions in the Pt-Pt bond distances which confirmed the results from *ex situ* XRD analysis. A potential excursion to 0.84 V *vs.* RHE showed that, in contrast to the Pt alloys, the Pt/C electrocatalyst exhibits a significant increase in the Pt *d*-band vacancies per atom. This increase, in Pt/C has been rationalized as being due to adsorption of OH species from the electrolyte following a Temkin isotherm behavior, which does not occur on the Pt alloys. Correlation of the electronic (Pt *d*-band vacancies) and geometric (Pt-Pt bond distance) with the electrochemical performance characteristics exhibits a volcano type behavior with the PtCr/C alloy being at the top of the curve. The enhanced electrocatalysis by the alloys therefore can be rationalized on the basis of the interplay between the electronic and geometric factors on one hand and their effect on the chemisorption behavior of OH species from the electrolyte.

The role of Pt/C and Pt alloys on the mechanism of the oxygen reduction reaction (ORR) has been investigated previously,[1-4] however the mechanism still remains elusive. One of the first investigations[1] of the ORR on Pt alloy electrocatalysts was in phosphoric acid; the effect of changes in the Pt-Pt interatomic distances, caused by alloying, was examined. The strength of the $[M\text{-}HO_2]_{ads}$ bond, the intermediate formed in the rate-determining step of the molecular dioxygen reduction, was shown to depend on the Pt-Pt bond distance in the alloys. A plot of the electrocatalytic activity *vs.* adsorbate bond strength exhibited a volcano type behavior.[5] It was shown that the lattice contractions due to alloying resulted in a more favorable Pt-Pt distance (while maintaining the favorable Pt electronic properties) for dissociative adsorption of O_2. This view was disputed by Glass *et al.*[2] in their investigation on bulk alloys of PtCr (the binary alloy at the top of the volcano plot) of different compositions. The latter investigation showed no activity enhancement for the ORR in phosphoric acid. This study therefore suggested the possibility of differences in electrochemical properties of bulk *vs.* supported alloy electrocatalysts (small particles of 35-85 Å). A recent study on supported PtCo electrocatalysts[4] revealed the possibility that particle termination, primarily at the <100> vicinal planes in the supported alloy electrocatalyst, is the reason for the enhanced ORR electrocatalysis (*i.e.*, <100> vicinal planes are more active than <111>). Paffett *et al.*,[3] attributed higher activities for the ORR on bulk PtCr alloys in phosphoric acid to surface roughening, and hence increased Pt surface area, caused by the dissolution of the more oxidizable alloying component Cr. In contrast to these findings on bulk alloys, the supported alloy electrocatalysts have been reported to retain their nonnoble alloying element in the electrode during long periods (6000-9000 h) of operation in phosphoric acid fuel cells (PAFCs)[6] and proton exchange membrane fuel cells (PEMFCs).[7]

Based on these previous investigations and in the context of the ORR mechanisms, the principle explanations for the enhanced ORR activity could be enumerated as being due to (*i*) modification of the electronic structure of Pt (5 *d*-orbital vacancies); (*ii*) changes in the physical structure of Pt (Pt-Pt bond distance and coordination number); (*iii*) adsorption of oxygen-containing species from the electrolyte on to the Pt or alloying element; and/or (*iv*) redox type processes involving the first row transition alloying element.[8]

One most powerful analytical technique which in principle can elucidate these different explanations is *in situ* x-ray absorption spectroscopy (XAS). The application of XAS to electrochemical systems has been reviewed recently.[9] The spectra consists of two parts, the near-edge part XANES (x-ray absorption near-edge structure) which gives chemical information and EXAFS (extended x-ray absorption fine structure) which gives the structural information. The XANES (±50 eV relative to the absorption edge) is comprised primarily of multiple scattering and transition-to-empty states in the vicinity of the Fermi level by low energy photoelectrons with relatively long mean-free paths. The XANES can provide information on the oxidation state from the size and shift in the edge-transition and on the coordination symmetry of ligands around the excited atom from the shape of the edge transition. For Pt, analysis of the XANES white lines at the L_3 and L_2 edge can yield information on the *d*-band vacancies. The EXAFS region is 40 to 1500 eV beyond the absorption edge and is caused by the modulation of the x-ray intensity due to backscattering by a small fraction of the backscattered photoelectron wave. This interference effect caused by single-scattering electrons with short mean-free paths provides information about the short-range atomic order (coordination number and bond distances). The present study focuses on the investigation of several Pt electrocatalysts alloyed with the first-row transition metals to elucidate the dependence of electrode kinetics of oxygen reduction on their electronic and structural properties. For this purpose *ex situ* or *in situ* electrochemical, XRD, and XANES and EXAFS techniques were used.

* Electrochemical Society Active Member.

Downloaded 09 Mar 2011 to 129.10.187.55. Redistribution subject to ECS license or copyright; see http://www.ecsdl.org/terms_use.jsp

Experimental

Electrodes and preparation of membrane electrode assembly.—Five carbon-supported binary Pt alloy electrocatalysts (PtCr, PtMn, PtFe, PtCo, and PtNi) were procured from Johnson-Matthey Inc., NJ. Based on previous investigations,[10,11] the electrocatalyst loading was chosen as 20% (by weight) metal on carbon; the Pt loading in the electrode (for both Pt/C and the Pt alloy electrocatalysts) was 0.3 mg cm^{-2} (confirmed by atomic absorption spectroscopy). All electrodes used in this study were prepared according to a procedure described elsewhere.[12]

As described in previous communications,[7,13,14] the electrodes were impregnated with Nafion solution (Nafion®-1100, 5% by weight, in a mixture of lower alcohols, Aldrich Chemical Company) using a brushing technique. This was followed by air-drying at 80°C and weighing to ensure a Nafion loading of approximately 0.6 mg cm^{-2}. An Asahi membrane (Acipex®-S1004, Asahi Chemical Industry, Japan) was pretreated by first heating in high purity water (Continental water purification system, Modulab Type 1), and second, in 5 volume percent (v/o) aqueous solution of H_2O_2 (J. T. Baker) for 1 h at 70 ~ 80°C to remove organic impurities. The membrane was then heated in 0.5*M* H_2SO_4 (J. T. Baker) at 70 to 80°C. Finally, the H_2SO_4 was removed by repeatedly treating it in boiling water. The electrodes were then hot-pressed to the membrane at 1000 psig pressure and 155°C for 90 s. This temperature was chosen because it is close to the glass-transition temperature of the membrane.

Assembly of single cell and its installation in the test station.—The membrane and electrode assembly (MEA) was incorporated in a single-cell test fixture. Details of the single-cell test fixture and the MEA assembly are given elsewhere.[14] A platinized Pt electrode located in the anode compartment served as the reference electrode. The single cell was then installed in the fuel cell test station.[14] The test station had provisions for temperature and pressure control, humidification of the reactant gases (hydrogen and oxygen), gas flow rate measurements, and measurements of half- and single-cell potentials as a function of current density. The electrical leads from the test station were connected to a programmable power supply (Hewlett-Packard Model 6033A), which was interfaced with an IBM/PS-2 computer for data acquisition, plotting, and analysis.

Electrode kinetic and cyclic voltammetric experiments.—Prior to the electrochemical performance evaluation, it was essential to attain the optimum operating conditions (with respect to conditioning of electrodes, water content of membrane, humidification conditions, and removal of organic impurities), because when a single cell is assembled the proton exchange membrane is in a dry state. For this purpose the cell was maintained at 50°C with the hydrogen and oxygen gases (1 atm) humidified at 60 and 55°C, respectively, while it was operated at a current density of 200 mA cm^{-2} for the first 24 h. After this period, the cell temperature was raised to 85°C, the reactant gas pressure to 5 atm, and the temperature in the H_2 and O_2 humidification bottles to 95 and 90°C, respectively. It was then operated for 8 h at a current density of 2 A cm^{-2}, for equilibration with the product water, to attain optimal water absorption conditions by the proton exchange membrane. Thereafter, the measurement of the *i*R-corrected Tafel plots for the ORR were made at 5 atm and 95°C with the oxygen and hydrogen gases being humidified at 100 and 105°C.

The cyclic voltammetry experiment was carried out using an argon flow through the working electrode (cathode, oxygen electrode) compartment and the electrodes were intially subjected to potential cycling (50 times) at 25 mV s^{-1}. The cyclic voltammogram (CV) was then recorded to determine the electrochemically active surface area. The potential was scanned between 120 mV to 1 V *vs.* RHE and sweep rates in the range 10 to 50 mV s^{-1} were used. For the measurement of the coulombic charge due to hydrogen adsorption or desorption lower sweep rates are preferred so as to minimize the pseudo-transmission line effects in the porous electrode. The electrochemically active surface area of the electrode was obtained using the charge required for hydrogen desorption from the Pt surface in the electrocatalyst.

X-ray diffraction.—The characteristics of the crystalline structure of supported Pt/C and binary Pt alloys (formation of superlattices, etc.) were determined using the powder XRD technique. The data was obtained using a Sintag automated diffractometer with a Cu-K_α radiation source. The powdered electrocatalyst samples were kept in a 2.5 × 2.5 cm × 1 mm quartz block. The powders were pressed onto the quartz block using a glass slide to obtain a uniform distribution. The diffractometer was interfaced with PDP 11/23 computer for data analysis and plotting. The 2θ Bragg angles were scanned over a range of 0 to 80°. The diffraction patterns were recorded and analyzed by com-

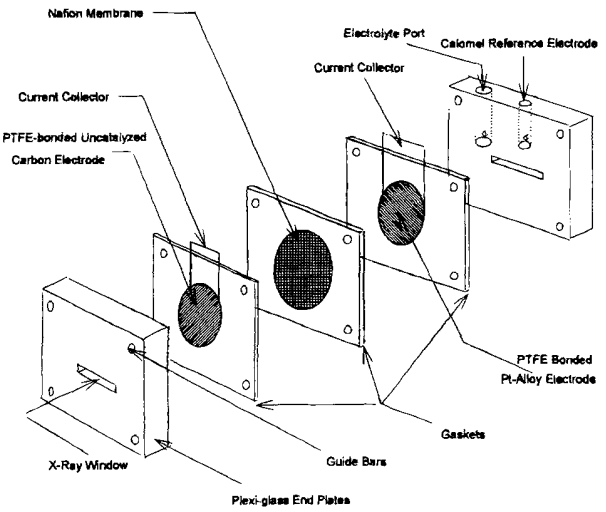

Fig. 1. Schematic diagram of the *in situ* electrochemical cell used to obtain the x-ray adsorption spectra.

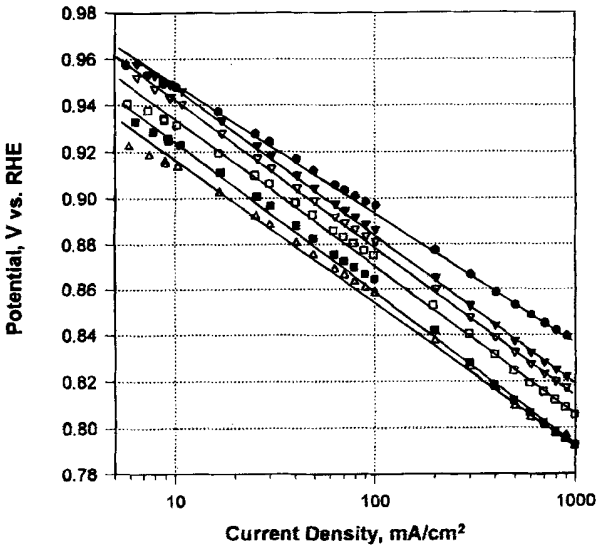

Fig. 2. *i*R-corrected Tafel plots for oxygen reduction in PEMFCs at 95°C and 5 atm pressure for Pt and Pt alloy electrocatalysts, Pt loading on electrodes 0.3 mg cm^{-2}. PtCr/C (●); PtMn/C (▽); PtFe/C (▼); PtCo/Co (□); PtNi/C (■); and Pt/C (△).

Downloaded 09 Mar 2011 to 129.10.187.55. Redistribution subject to ECS license or copyright; see http://www.ecsdl.org/terms_use.jsp

Table I. Electrode kinetic parameters for oxygen reduction at Pt and Pt alloy electrocatalysts in PEMFCs at 95°C and 5 atm pressure. Pt loading in electrodes 0.3 mg cm^{-2}.

Electrocatalyst	E_o (mV)	b (mV/dec.)	R (Ω cm^2)	i_o (mA cm^{-2}) (10^4)	i_{900mV} (mA cm^{-2})	$E_{10mAcm^{-2}}$ (mV)	Roughness factor (cm^2 cm^{-2})	i_o[a] (mA cm^{-2}) (10^5)
Pt/C	982	63	0.14	3.46	22.1	915	61	0.56
PtMn/C	995	64	0.10	6.26	40.1	945	48	1.30
PtCr/C	1005	62	0.09	7.15	83.8	951	50	1.43
PtFe/C	1001	63	0.10	6.94	50.4	948	56	1.36
PtCo/C	990	65	0.11	5.87	37.2	935	49	1.19
PtNi/C	988	64	0.11	4.86	26.4	924	48	1.01

[a]Normalized with respect to the electrochemically active surface area.
The parameters E_o, b, and R are defined for Eq. 1 and 2 in the text.

paring them with standard powder diffraction data such as Joint Commission on Powder Diffraction Standards (JCPDS) powder diffraction patterns (National Institute of Standards and Technology, NIST). All the powder diffraction patterns were obtained using an internal standard of Al powders [20 μm spherical particles, AESER (Johnson-Matthey, Inc.)] for calibration of XRD line positions and for particle size estimations. The presence of this internal standard was evident from its primary diffraction line <200> at the 2θ position of 44.6° and from smaller diffraction lines such as those at 66° (<220> diffraction line) in all the powder diffraction patterns.

In situ XANES and EXAFS investigation.—The XAS measurements were carried out at the National Synchrotron Light Source (NSLS), Brookhaven National Laboratory (BNL), using the NIST beam line X23A2. The monochromator was a two-crystal (Si <311>, interplaner distance 1.9650 Å) upwardly reflecting fixed exit Golovchenko-Cowan design[15,16] with an energy resolution ($\Delta E/E$) of 2×10^{-4}. Based on the monochromator and overall beam line configuration, the presence of second harmonics was negligible. The absence of second harmonics was confirmed however by taking absorption spectra on sample containing elements which had absorption edges at approximately twice the energy of the test samples. Hence in the Pt L_3 edge an Rh K-edge reference ($RhCl_3$) sample was used. Similarly for the Cr and Mn K-edges, Au and Pb L_3 edges were used. The Ta and Bi L_1 edges were used to test for second harmonics at the Co and Ni K-edges. The *in situ* XAS on the electrocatalysts was conducted both in transmission and fluorescence modes. The data acquisition setup in the transmission mode comprised of three 12 in. ionization chamber detectors [incidence (I_o), transmittance (I_t) and a reference (I_{ref}) detector]. The reference channel was primarily for internal calibration of the edge positions and was used in conjunction with pure foils of the respective elements. In the fluorescence mode, edge positions were first established using the appropriate reference foil of the pure element in the transmission mode followed by switching to the fluorescence data acquisition mode. The fluorescence mode however was used only for the measurement of Cr K-edge XANES. Measurements at all other element edges were carried out using the transmission mode. The gases used in the detectors depended on the element being examined. For the Ni K-edge, N_2 was used in all the chambers. For Pt L_3 and L_2 edges, N_2 was used in the I_o and I_{ref} chambers, in the I_t chamber a mixture of 50% N_2 and Ar was used. For Cr and Mn K-edges, 80% He and 20% N_2 gas mixtures were used in the I_o detector chamber. Composition of gases in the I_o chamber for Fe and Co K-edges was 50% He and 50% N_2. For the Mn, Fe, and Co K-edges, the I_t and I_{ref} chambers were filled with 100% N_2. For the Cr K-edge the I_{fls} (fluorescence) chamber had 100% He. As shown in Fig. 1 the *in situ* electrochemical cell was designed for XAS data acquisition in both transmission and fluorescence modes. The cell comprised of Plexiglas end plates with windows for passing x-ray beam and contained channels for incorporation of a calomel reference electrode with a built in Luggin capillary in contact with the working electrode (Pt/C or the binary Pt alloy electrodes). The saturated calomel reference electrode contained a special arrange-

Table II. Structural characteristics of the Pt and Pt alloy electrocatalysts, as obtained from XRD studies.

Electrocatalyst	Secondary phase contribution (%)	Lattice parameter Pt-Pt bond distance, (Å)	Average particle size (Å)
Pt/C	5	3.927 (2.777)	35
PtMn/C	3	3.898 (2.756)	69
PtCr/C	9	3.873 (2.738)	57
PtFe/C	2	3.866 (2.733)	58
PtCo/C	6	3.854 (2.725)	69
PtNi/C	7	3.812 (2.695)	58

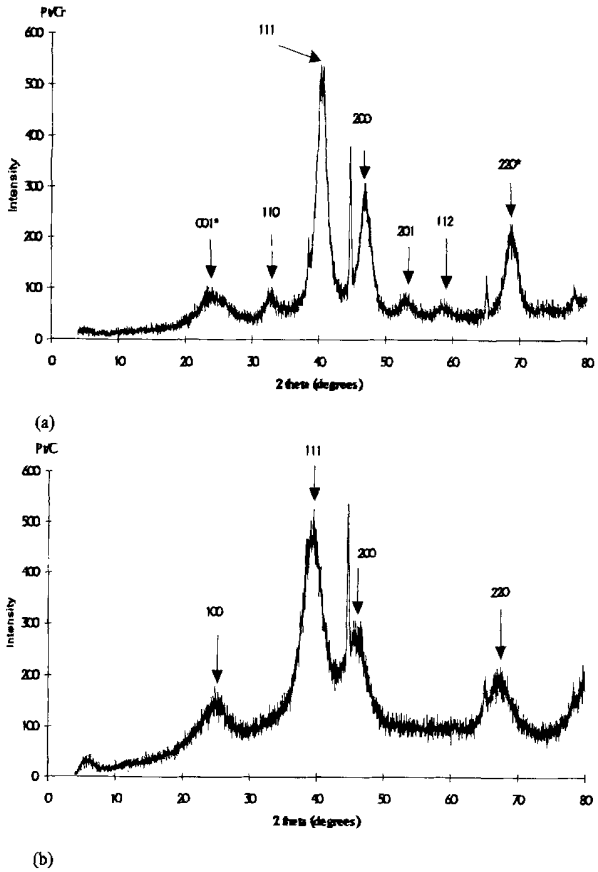

Fig. 3. XRD pattern for (a) PtCr/C electrocatalyst. Primary phase is Ll_2 type with fcc lattice. Contribution from secondary phase {*}(Ll_0 type with tetragonal lattice structure) is ~9% and (b) Pt/C electrocatalyst.

Downloaded 09 Mar 2011 to 129.10.187.55. Redistribution subject to ECS license or copyright; see http://www.ecsdl.org/terms_use.jsp

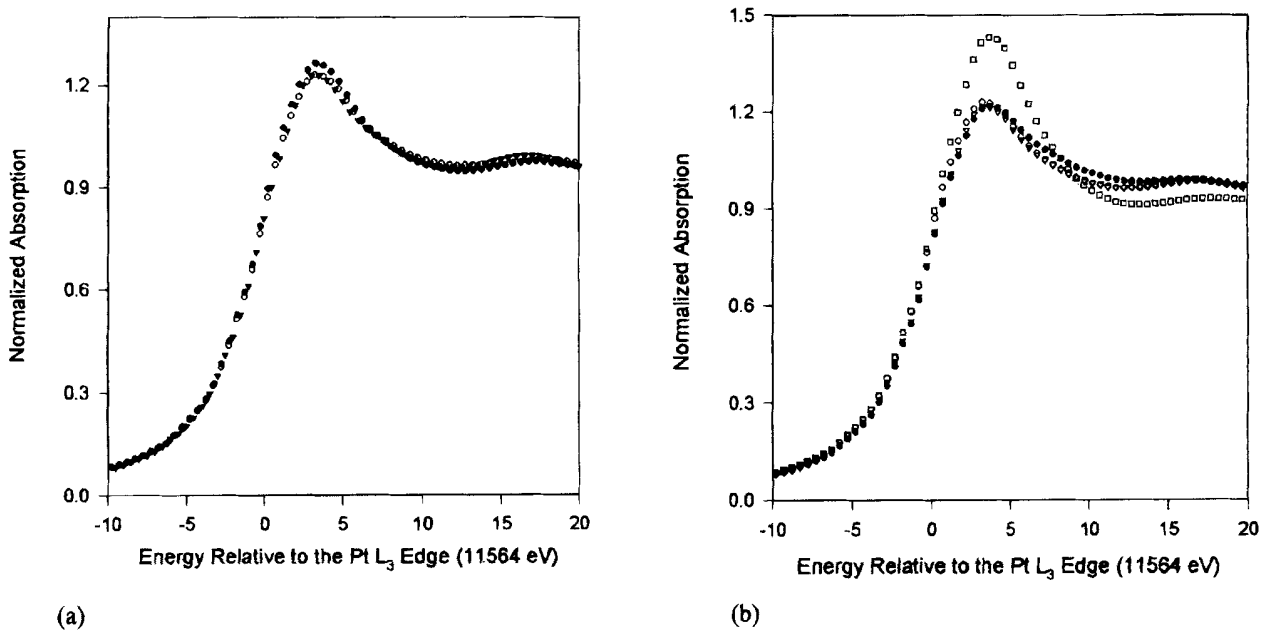

Fig. 4. Comparison of Pt L_3 XANES for Pt/C electrocatalyst at (a) 0.54 V in 1*M* H_2SO_4 (●) and 1*M* $HClO_4$ (▼) relative to a Pt reference foil (○), note the slight increase of the white line in H_2SO_4 and (b) in 1*M* $HClO_4$ at 0.0 (●); 0.54 (▽), and 1.14 (□) V relative to a Pt reference foil (○), note the broadening of the Pt L_3 white line at 0.0 V and the large increase at 1.14 V.

ment of a double Nafion salt bridge to avoid chloride contamination. The anode and cathode compartments were separated using an electrolyte barrier comprised of Nafion 117 (Du Pont Chemical Co., DE) proton exchange membrane. The anode comprised of an uncatalyzed carbon electrode to avoid any interference in the transmitted working electrode signal. The test electrodes were prepared by a vacuum table paper making technique[17] and contained 12% polytetrafluoroethylene (PTFE) binder. The electrodes were formulated to yield an absorption length, $\mu x \approx 1$ at the Pt L_3 edge. In most cases, this yielded adequate step-heights for the XAS measurements at the respective transition element K-edge in the transmission mode. Only for Cr was it necessary to resort to fluorescence measurements. Prior to fabrication of these electrodes, the Pt/C and binary Pt alloy electrocatalysts were soaked in 2*M* KOH (PtCr/C) or 1*M* $HClO_4$ (all others) to remove any residual oxides and unalloyed first-row transition metal elements. Since XAS is a bulk averaging technique, it is difficult to analyze the data when the element of interest is present in more than one chemical form or phase. For the same reason, the success of *in situ* measurements depended on ensuring that every part of the electrode under study was electroactive since any unused electrocatalyst could be in different chemical states and thus yield more complicated spectra. For this purpose all electrodes were soaked in 1*M* $HClO_4$ (the test electrolyte) for 24 h prior to XAS analysis. This acid was selected because of minimum adsorption of its anion. The electrocatalytic studies on the Pt and its alloys were made in the PEMFCs. The electrolyte in contact with the electrode was a perfluorinated sulfonic acid, the anion of which does not adsorb on the electrocatalyst.[17]

The potential control for the *in situ* XAS measurements was carried out using a potentiostat (Stonehart Associates, Model No. BC-1200) and a function generator (Princeton Applied Research Model PAR-175). XAS data were first recorded at the Pt L_2 and L_3 edges and then at the K-edge of the respective alloying element. The measurements were first made at the open-circuit potential and then at potentials of −0.24, 0.0, 0.3, and 0.6 V *vs.* saturated calomel electrode (SCE) (or 0.0, 0.24, 0.54, and 0.84 V *vs.* RHE).[a] The potential was changed from one value to the next at a sweep rate of 1 mV $s.^{-1}$ The K-edge XAS measurements for the alloying element also were carried out at 0.9 V *vs.* SCE (1.14 V *vs.* RHE) to check for its stability.

[a] Note that all the potentials in this article are given with reference to the reversible hydrogen electrode for uniformity.

Results and Discussion

Electrode kinetic parameters for oxygen reduction.— Figure 2 shows that the half-cell potential (E) *vs.* current density (i) data fit the equation[11]

$$E = E_o - b \log i - Ri \quad [1]$$

where

$$E_o = E_r + b \log i_o \quad [2]$$

In Eq. 1 and 2, i_o is the exchange current density for oxygen reduction, b is the Tafel slope, E_o is the reversible potential for the oxygen electrode reaction, and R represents the resistance (predominantly the ohmic resistance of the electrolyte) responsible for the linear variation of potential *vs.* current density plot. Equation 1 is valid to the end of the linear region of the half-cell potential *vs.* current density plot. At high current densities, the departure of the E *vs.* i data from Eq. 1 is due to the rapidly increasing contributions of mass-transport overpotentials. The parameters E_o, b, and R were evaluated by a nonlinear least square fitting of Eq. 1 to the experimental data. Using the R values, the iR-corrected Tafel plots [($E + iR$ *vs.* log i)] were constructed.

As evident from Fig. 2 all five binary Pt alloys show enhancement of electrocatalytic activity for ORR, as compared to that on Pt/C electrocatalyst (all electrodes contained the same Pt loading, 0.3 mg cm^{-2}). The extent of the enhancement is expressed quantitatively by the values of electrode kinetic parameters obtained from half-cell data (Table I). A two- to threefold activity enhancement in terms of the geometric surface area of the electrode is indicated by the values of current density at 900 mV (Table I). A similar trend is observed for the values of exchange current density, and the potential at 10 mA cm^{-2} (solely, activation controlled region). The electrocatalytic activities decrease in the order PtCr/C > PtFe/C > PtMn/C > PtCo/C > PtNi/C > Pt/C. The electrocatalytic activity for ORR on the Pt/C and the binary alloys of Pt also were calculated on a true surface area basis (electrochemically active surface area). The electrochemically active surface areas were obtained from the hydrogen desorption regions of the cyclic voltammograms for the Pt/C and the binary alloys of Pt.

Downloaded 09 Mar 2011 to 129.10.187.55. Redistribution subject to ECS license or copyright; see http://www.ecsdl.org/terms_use.jsp

The contribution of the alloying element to the roughness factor however was difficult to discern and thus it is assumed to be negligible. In the cyclic voltammetric experiments the potential range scanned was between 120 mV and 1.2 V *vs.* RHE at a scan rate of 25 mV s^{-1} with the cell operating conditions of 95°C and 5 atm pressure. The coulombic charge for the desorption of atomic hydrogen (area under the anodic peak minus the double-layer charge at 0.4 V *vs.* RHE) was used to evaluate the roughness factor of the electrode, assuming a value of 220 μC cm^{-2} for the oxidation of atomic hydrogen on a smooth Pt surface. Table I shows the value of exchange current density based on both the geometric as well as the true surface area; electrocatalytic enhancements for ORR to the extent of two- to threefold are indicated on a true surface area basis (the highest performance is shown by the PtCr/C alloy). The trends of electrocatalytic enhancement by the alloys, on a true surface area basis, are similar to those based on geometric areas.

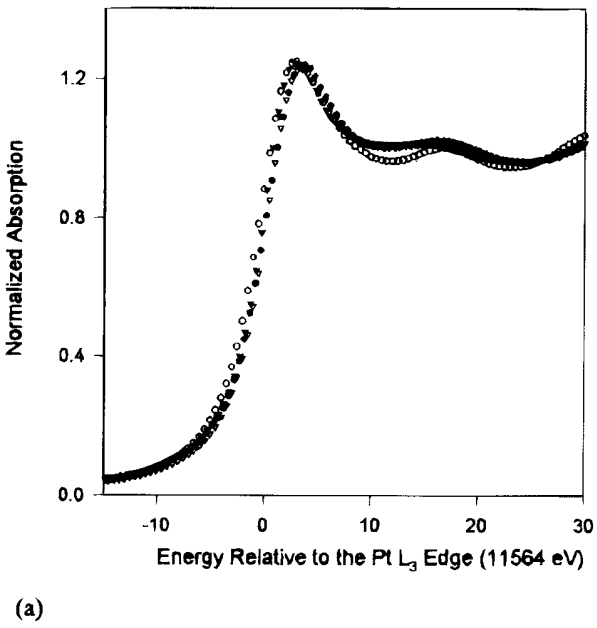

Fig. 5. XANES spectra at the Pt L_3 edge for (a) PtCr/C (●), PtMn/C (▽), PtFe/C (▼) and (b) Pt/C (△), PtCo/C (□), PtNi/C (■) relative to a Pt reference foil (○) at 0.54 V in 1*M* $HClO_4$.

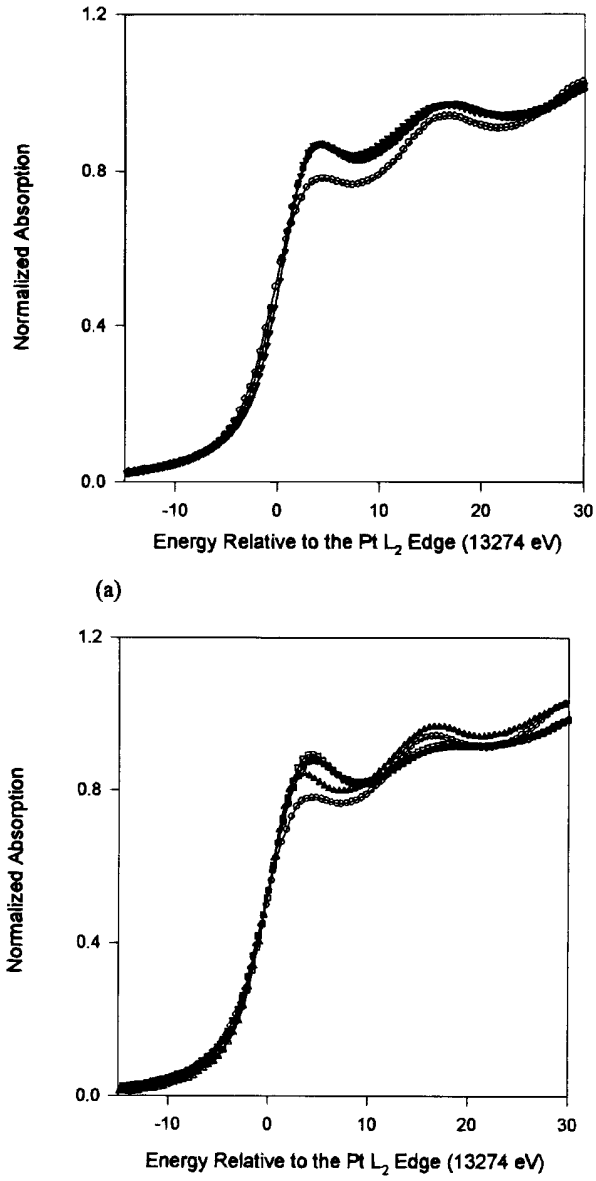

Fig. 6. XANES spectra at the Pt L_2 edge for (a) PtCr/C (●), PtMn/C (▽), PtFe/C (▼) and (b) Pt/C (△), PtCo/C (□), PtNi/C (■) relative to a Pt reference foil (○) at 0.54 V in 1*M* $HClO_4$.

XRD analysis, crystalline structure of alloys.—Comparison of the XRD patterns with those of the standard JCPDS powder diffraction data base and Ref. 18-23 shows that the PtMn/C, PtCr/C, PtFe/C, PtCo/C, and PtNi/C alloys form intermetallic crystalline structures, the primary superlattice phase being of the type Pt_3M (where M is the first-row transition alloying element) possessing an LI_2 type lattice with an fcc structure. Indications of a secondary phase of the type PtM possessing an LI_0 type lattice with tetragonal structure is also evident (represented by an asterisk on the respective diffraction line). The extent of contribution of this secondary phase (Table II), was estimated by the intensity of the diffraction lines due to the PtM phase [such as <001> and <220> diffraction lines in the PtCr/C powder diffraction pattern (Fig. 3a)]. The 2θ positions of the <100>, <111>, <200>, and <220> powder diffraction lines for the Pt/C electrocatalysts compare well with the standard JCPDS powder diffraction files and Ref. 18 and indicates that the electrocatalyst Pt/C has fcc lattice similar to bulk Pt (Fig. 3b). The lattice parameters for the Pt alloys, based on the Pt_3M type fcc lattice (Table II), reveal contractions, in comparison to that for the Pt/C electrocatalyst. The

Downloaded 09 Mar 2011 to 129.10.187.55. Redistribution subject to ECS license or copyright; see http://www.ecsdl.org/terms_use.jsp

Table III. Electronic and geometric parameters for the Pt and Pt alloy electrocatalysts as obtained from *in situ* XANES and EXAFS experiments at 0.54 and 0.84 V *vs.* RHE.

Electrocatalyst	Electrode potential (0.54 V *vs.* RHE) $(h_J)_{t,s}$	Pt-Pt (R) (Å)	Pt-Pt (N)	Electrode potential (0.84 V *vs.* RHE) $(h_J)_{t,s}$	Pt-Pt (R) (Å)	Pt-Pt (N)
Pt/C	0.329	2.77	8.7	0.370	2.77	6.8
PtMn/C	0.331	2.76	7.5	0.344	2.76	8.3
PtCr/C	0.360	2.71	6.1	0.358	2.71	6.1
PtFe/C	0.368	2.70	6.7	0.370	2.71	6.5
PtCo/C	0.401	2.68	6.9	0.390	2.68	7.6
PtNi/C	0.409	2.68	9.1	0.404	2.68	9.5

$(h_J)_{t,s}$, Pt d-orbital vacancy per atom.
R, interatomic distance.
N, coordination number around the first coordination shell.

lattice parameters decrease in the order Pt/C > PtMnC > PtCr/C > PtFe/C > PtCo/C > PtNi/C (Table II). The particle sizes, based on x-ray line broadening, were estimated using the Scherrer equation[24] and the linewidth at half-maximum intensity, corrected for instrument-broadening, was obtained using the Warrens equation.[25] The particle sizes were obtained from peak broadening of <111> diffraction line of the primary phase in the Pt and Pt alloys, relative to the <220> diffraction line for 20 μm spherical particles of Al powder used as an internal standard (2θ peak position at 44.6°). Table II shows that particle size increases due to alloying in the order of Pt/C < PtCr/C < PtFe/C, PtNi/C < PtCo/C, PtMn/C.

XAS Investigations.—XANES and EXAFS data analysis.—One significant aspect of XANES analysis is that it can provide important information on the Pt d-band vacancies. The d-band vacancies are derived from an analysis of the Pt L_3 and L_2 white lines. The respective L_2 and L_3 edges are due to excitation of $2p_{1/2}$ and $2p_{3/2}$ electrons. These electrons can undergo transitions to empty states in the vicinity of the Fermi level. Since the dipole selection rules in XANES region restrict transitions to $\Delta L = \pm 1$ and $\Delta J = 0, \pm 1$ (L and J are the orbital angular and the total angular quantum numbers) the transitions to the d-orbitals are most strongly favored.[26] For Pt, it has been shown that final states with $J = 5/2$ contribute 14 times more than those with $J = 3/2$.[27,28] The L_3 transitions ($2p_{3/2}$ to $5d_{5/2}$) are thus more favored, by selection rules, than the L_2 transitions ($2p_{1/2}$ to $5d_{5/2}$). The intensity of the L_3 and to a lesser extent the L_2 peaks increase with increase in Pt d-band vacancy. From the difference in areas under the Pt L_3 and L_2 absorption edges between the sample (Pt/C and Pt alloy electrocatalyst) and a pure Pt reference foil, the fractional change in the number of d-band vacancies relative to the reference material (f_d) can be estimated using the relation

$$f_d = \frac{(\Delta A_3 + 1.11\Delta A_2)}{(A_3 + 1.11A_2)_r} \quad [3]$$

where ΔA_3 and ΔA_2 are expressed by

$$\Delta A_2 = (A_{2s} - A_{2r}) \text{ and } \Delta A_3 = (A_{3s} - A_{3r}) \quad [4]$$

The terms A_2 and A_3 represent the areas under L_2 and L_3 absorption edges of the sample (s) and reference (r) material. The total number of unoccupied d-states, characterized by the total angular moment J [$(h_J)_{total} = h_{3/2} + h_{5/2}$] for pure Pt, has been evaluated from band structure calculations to be 0.3.[27,28] Therefore the d-band vacancies of Pt in the sample can be evaluated using the equation

$$(h_J)_{total,sample} = (1.0 + f_d)\,(h_J)_{total,reference} \quad [5]$$

Fundamentals of this methodology are described in detail by Mansour *et al.*[29,30] Previous studies have focused on the determination of the Pt d-band occupancy in alumina and titania-supported Pt catalyst[29-31] and on the role of small Pt clusters in Y zeolites.[32] This technique therefore constitutes a new way of examining the role of the alloying element in binary Pt alloys in terms of the d-band occupancy of Pt and hence is used in this investigation to elucidate the differences in ORR electrocatalysis on Pt alloys *vs.* Pt/C electrocatalyst.

The data analysis package used for XANES was the University of Washington data analysis program.[33] The XANES spectra were first subjected to background removal by fitting the pre-edge data to a Victoreen type formula over a range of 200 to 40 eV below the edge (this range was the same for all the samples at both the alloying element and the Pt edges), followed by extrapolation over the energy range of interest and subtraction from the data. After removal of background contributions, the spectra were corrected for edge-shifts using the second derivatives of the inflection points of data from the reference channel (5 μm Pt or alloying element reference foil). The procedures used for normalization were similar to those described by Wong *et al.*[34] The normalization value was chosen as the absorbance at the inflection point of one EXAFS oscillation. The spectra were thus normalized by dividing each datum point by the normalization value. The edge areas (A_{2s} and A_{3s}) were calculated by numerical integration using Simpson's rule. The spectral window for such an integration was −10 to 13 eV, relative to the absorption edge. The denominator in Eq. 3, $(A_3 + 1.11\,A_2)_r$ was determined according to the procedure of Brown *et al.*[27] All the areas (ΔA_2, ΔA_3, A_{3r}, and A_{2r}) were normalized by the x-ray cross section at the edge-jump and the density of the absorbing material.[35]

The EXAFS data analysis involved using computer algorithms developed by Koningsberger and co-workers.[36,37] The first step in the analysis of an EXAFS spectrum is the extraction of the normalized EXAFS data from the measured XAS spectra. The raw data were initially subjected to a pre-edge subtraction (−200 to −50 eV relative to the Pt L_3 edge) using a second-order polynomial. The use of a second-order polynomial instead of a Victoreen type expression stemmed from the former's ability to more adequately handle contributions of ionization chambers over the longer energy range involved in EXAFS analysis. This was specially relevant due to dissimilar spectral response of the detectors when using different gas compositions.[36] The background removal in the postedge region was conducted using cubic spline functions over the energy range of +20 to +1500 eV at the Pt L_3 edge. The normalization factor in the EXAFS analysis was taken as the height of the edge-jump in the threshold region. This was obtained by determining the difference in the heights of the extrapolated backgrounds in the pre-edge and postedge regions at the threshold region of 50 eV above the absorption edge. The isolated EXAFS spectra at the Pt L_3 edge for the supported Pt and Pt alloy electrocatalysts were of high quality and did not require any deglitching. The Fourier filtering and analysis of the EXAFS spectra were conducted according to the procedure described in detail elsewhere.[38-40] The most comprehensive analysis of the EXAFS spectra is typically done following an inverse Fourier transform to allow analysis of k-space amplitudes and isolation of the primary coordination shells of interest. The isolation of a limited

Downloaded 09 Mar 2011 to 129.10.187.55. Redistribution subject to ECS license or copyright; see http://www.ecsdl.org/terms_use.jsp

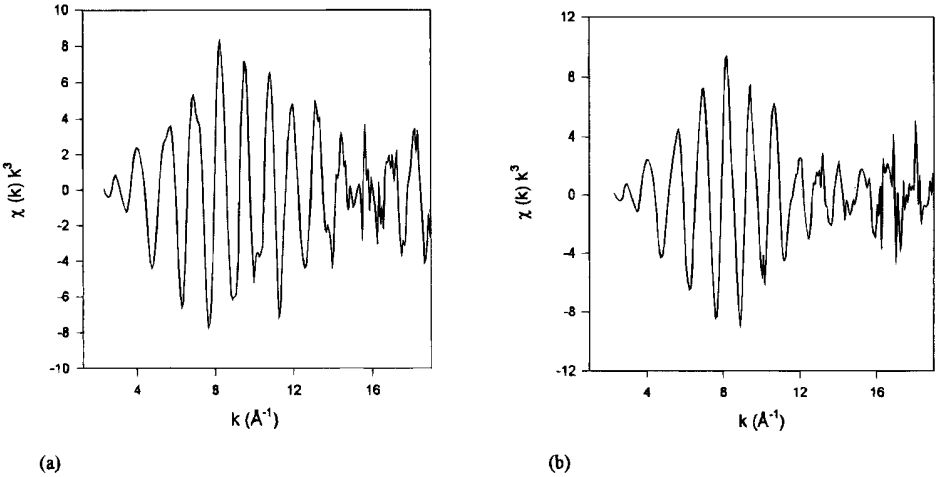

Fig. 7. EXAFS spectrum at the Pt L_3 edge recorded at 0.54 V for (a) PtCr/C alloy and (b) PtMn/C alloy.

number of shells in r-space allows, as part of the inverse Fourier tranform, a reduction in the number of parameters that must be determined. The analysis of the EXAFS spectrum for the alloys was therefore carried out as one, two, and three shell fits using an iterative least square fitting technique.[41] For fitting the sample data from the Pt/C and the binary Pt alloys under *in situ* conditions, phase and amplitude parameters from standard materials as well as those calculated theoretically using University of Washington FEFF programs (Version 4.08) were employed.[42] The standard reference material used in this work was the liquid N_2 data for a pure Pt foil (5 μm thick) and the octahedrally coordinated complex, $Na_2Pt(OH)_6$, for the Pt-Pt and Pt-O phase and amplitude parameters, respectively. The Pt-M phase and amplitude parameters were obtained from theoretical calculations using the FEFF programs[42] based on Cartesian coordinate inputs for an fcc lattice structure (assumption based on previous results using XRD). In these theoretical calculations, an S_o^2 value of 0.87 was used throughout.

Electronic and structural characteristics from in situ XAS investigations.—As stated in the Experimental section, the XAS studies were conducted on the test electrodes in a liquid electrolyte rather than at their interfaces with proton exchange membrane, to ensure that all the electrocatalyst particles were electroactive. For this purpose, perchloric acid was used as the electrolyte of choice because of minimal anion adsorption of this acid on Pt (perfluorinated sulfonic acid, the anion in the proton exchange membrane, possesses similar properties). Preliminary results using other liquid electrolytes such as H_2SO_4 exhibited interference in the Pt L_3 white line due to the adsorption of HSO_4^- species (Fig. 4a). This interference was not only observed at the double-layer region (Fig. 4a) but over the entire range of potentials, including a potential as low as that at which hydrogen evolution occurs. Detailed XANES and EXAFS analyses at 0.54 V (double-layer region) provided the desired potential region for comparing the different Pt alloys in terms of electronic and geometric parameters with those of the Pt/C electrocatalyst, without interference from any type of ionic adsorption or other effects (Fig 4b). Besides this, detailed XANES and EXAFS analyses were conducted at 0.84 V, since this potential lies in the activation controlled region of the Tafel polarization plot for ORR. The electronic and geometric parameters obtained from XAS analysis at this potential were of interest in terms of their comparison with the corresponding values at the double-layer region. Figures 5 and 6 show the *in situ* XANES of Pt L_3 and L_2 edges at 0.54 V (after necessary steps of background removal, edge correction, and normalization) for the Pt/C and the five binary alloys of Pt. As evident from these figures, the magnitude of the white line determined at a potential in the double-layer region (0.54 V) is greater for the alloys (with the exception of PtMn/C) as compared to the Pt/C electrocatalyst. This is evident from the broadening of the white line for the PtCr/C and an increase in the white line intensity exhibited by PtFe/C, PtCo/C, and PtNi/C alloys relative to Pt/C electrocatalyst at the Pt L_3 edge (Fig. 5). The calculated values of the Pt d-band character, evaluated from the areas under the Pt L_3 and L_2 edges, are enumerated in Table III. The order of increase in the value of the Pt d-band vacancies per atom follows the trend Pt/C, PtMn/C < PtCr/C < PtFe/C < PtCo/C < PtNi/C. This trend shows that with the exception of PtMn/C alloy there is an increase in the d-band vacancy of Pt (5 d-orbital) and that this increase depends on the electron affinity of the alloying element. The reason for the PtMn/C alloy to be an exception is due primarily to the stable $3s^24d^5$ electronic configuration of Mn. The effect of the alloying element on the Pt-Pt bond distance was obtained by analyzing the Fourier transform of the EXAFS at the Pt L_3 edge. Figure 7 shows the representative plot for the isolated EXAFS spectrum at the Pt L_3 edge for the PtCr/C and PtMn/C alloys at a potential of 0.54 V. The EXAFS analysis involved Fourier filtering of the isolated EXAFS spectra (Pt L_3 edge) using k-space windows (Δk range) as described in Table IV. The correspond-

Table IV. Fourier transformation ranges of the forward and inverse transforms (k^3 weighted) for Pt/C and Pt alloy electrocatalysts at the double-layer and oxygen reduction regions.

	(0.54 V *vs.* RHE)		(0.84 V *vs.* RHE)	
Electrocatalyst	Δk (Å^{-1})	Δr (Å)	Δk (Å^{-1})	Δr (Å)
Pt/C	3.49-14.23	1.40-3.05	3.26-14.15	1.3 -3.04
PtCr/C	3.15-14.71	1.41-3.41	3.15-14.71	1.50-3.41
PtMn/C	3.70-14.22	1.21-3.61	2.73-17.42	1.04-3.52
PtFe/C	3.45-17.14	1.50-3.40	3.68-17.45	1.50-3.40
PtCo/C	3.22-14.61	1.50-3.50	3.22-14.76	1.50-3.40
PtNi/C	3.55-14.64	1.50-3.50	3.55-14.85	1.30-3.50

Fourier transformation ranges of the forward and inverse transforms for reference standards.

Reference Standard	Δk (Å^{-1})	Δr (Å)	N_{ref}	R_{ref}
Pt foil (Liq. N_2 Temp.) (Pt-Pt standard)	3.55-19.22	1.04-3.52	12	2.774
$Na_2Pt(OH)_6$; (Liq. N_2 Temp.) (Pt-O standard)	3.52-17.18	1.05-2.40	6	2.052
Pt-Cr standard (FEFF program)	3.30-19.50	1.40-3.10	12	2.774
Pt-Mn standard (FEFF program)	3.30-19.45	1.40-2.92	12	2.774
Pt-Fe standard (FEFF program)	3.14-18.14	1.45-2.95	12	2.774
Pt-Co standard (FEFF program)	2.92-19.17	1.40-3.40	12	2.774
Pt-Ni standard (FEFF program)	2.55-19.25	1.50-3.50	12	2.774

Downloaded 09 Mar 2011 to 129.10.187.55. Redistribution subject to ECS license or copyright; see http://www.ecsdl.org/terms_use.jsp

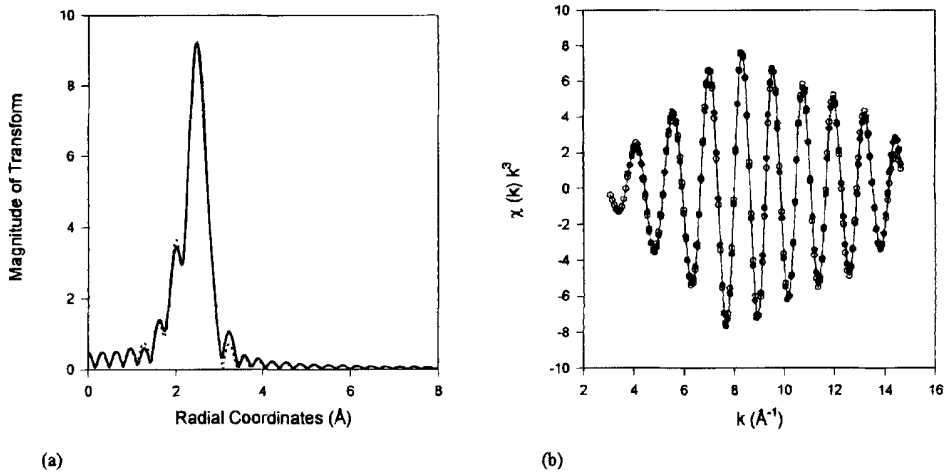

Fig. 8. A two-shell fit (Pt-Pt and Pt-Cr) for the EXAFS of PtCr/C sample at 0.54 V in (a) *r*-space and (b) *k*-space. The fits are k^3 weighted with the sample data denoted by [(···) in *r* and (○) in *k*-space] and the fit data by [(—) in *r* and (●) in *k* space].

ing Fourier transform allowed isolation of a limited number of shells by an inverse Fourier transform for analysis using iterative least square fitting with the experimentally and theoretically derived phase and amplitude parameters from standards. The windows in *r*-space used to perform the inverse Fourier transform for the Pt and Pt alloys are given in Table IV. The approach taken in fitting the data was to select the simplest model first and attempt to fit the data. Thus at 0.54 V the Pt/C data was fit using a simple Pt-Pt coordination shell. Similarly the Pt alloy data were fit to a two-shell model consisting of Pt-Pt and Pt-M contributions. At 0.54 V this approach was successful. Examples of fits in the *k* and *r*-space are given in Fig. 8, which shows the representative two-shell fits for the PtCr/C alloy. The EXAFS analysis therefore indicated no Pt-O interactions in any of the samples at 0.54 V. The Pt/C data could be fit to a simple Pt-Pt single-shell model. The alloy data could be fit to a two-shell Pt-Pt, Pt-M model. Since there are no Pt-O interactions, it can be concluded that all the changes in the *d*-orbital vacancies are attributable to the alloying element. Tables V and VI show the results of this *in situ* EXAFS analysis. The error limits in the EXAFS analysis (Tables V-VII) were obtained according to procedure described elsewhere.[43] For single-shell fits the limits of error ranged between 1 and 8% for *N* and 0.005 to 0.01 Å for *R*. For two-shell fits the error limits were typically in the range of 5 to 14% for *N* and 0.007 to 0.012 Å for *R*.

Comparison of the Pt-Pt bond distances indicates a contraction as a result of alloying. The Pt-Pt bond distances determined from XRD and *in situ* EXAFS analysis at 0.54 V exhibit good agreement (Tables II and III) and follow the same trend. In addition there is an inverse relationship between the Pt-Pt bond distance in the electrocatalysts and their Pt *d*-band character (Table III). The coordination numbers obtained for the Pt/C and Pt alloy electrocatalyst were lower than those expected for corresponding bulk samples. The primary reason for this behavior is based on particle sizes of the Pt and Pt alloy crystallites. As a result, the Pt/C electrocatalyst exhibits a coordination number of ~9 instead of 12 (bulk sample). Similarly the coordination numbers around Pt in the alloys (sum of Pt-Pt and Pt-M) range between ~9 and 11 instead of 12 for the bulk phase.

Figures 9 and 10 show the Pt L_3 and L_2 XANES spectra at 0.84 V (oxygen reduction region) for carbon supported Pt and Pt alloy electrocatalysts. Comparison of Pt L_3 XANES (Fig. 5 and 9) at the two potentials of 0.54 and 0.84 V, reveal significant increase in the intensity of the Pt L_3 white line for Pt/C electrocatalyst. Table III provides a measure of the extent of increase in the Pt *d*-band vacancy per atom for Pt/C electrocatalyst as a result of this change in potential. In Pt alloys, however, such an increase in the Pt *d*-band vacancy does not occur (with the exception of PtMn/C alloy, wherein a small increase was observed). The increase in the value of Pt *d*-band vacancy for the Pt/C electrocatalyst in contrast to those in the Pt alloys can be rationalized on the basis of results from EXAFS analysis at both 0.54 and 0.84 V. Comparison of the Fourier transforms of the EXAFS spectra at 0.54 and 0.84 V for Pt/C electrocatalyst (Fig. 11a) shows peaks due to presence of oxygenated species at low *R* values (<2 Å) at 0.84 V. This also causes a decrease in the number of Pt-Pt interactions at 0.84 V as shown by the lower magnitudes of transformation at this potential (Fig. 11a). In contrast to this a similar comparison for the Pt alloys shows virtually no difference as a result of this potential change. This is illustrated by the representative plot for PtCr/C alloy in Fig. 11b. This fact can be further illustrated in Fig. 12a, which shows a single-shell Pt-Pt fit of the Pt/C sample data at 0.84 V. This figure shows deviations from the fit at low *R* values which are attributed to the presence of chemisorbed oxygen on the Pt/C electrocatalyst. In contrast, a two-shell fit, using the Pt-Pt and the Pt-O standards, gives an excellent fit (Fig. 12b), thus confirming the earlier hypothesis. Table V lists the corresponding results of the EXAFS analysis. These results on the Pt/C electrocatalysts are in agreement with the results from previous XAS investigations on the Pt/C electrocatalysts.[44] Further, cyclic voltammetric experiments together with theoretical and experimental investigations of the ORR mechanism[45,46] show the increase of coverage by OH or O species at potentials higher than 0.80 V and the effect of a Temkin type adsorption isotherm on the electrode kinetic parameters. The contrasting results on the Pt alloys (with the exception of PtMn/C alloy) appears to be due to the electronic properties of Pt remaining practically identical at the potentials of 0.54 and 0.84 V. This is confirmed in Pt alloys, since the Pt L_3 EXAFS data at 0.84 V could still be fit to a simple two-shell Pt-Pt and Pt-M fit. It was not necessary to include a Pt-O contribution indicating insignificant oxidation of Pt at 0.84 V. Attempts for three-shell fits with the Pt-Pt, Pt-M, and Pt-O standards at 0.84 V failed to provide a better fit for all the binary Pt alloys including the PtMn/C alloy. Figure 13 illustrates the quality of two-shell fits in the *k* and *r*-space for PtCr/C alloy at 0.84 V. The corresponding values of *N*, *R*, $\Delta\sigma^2$, and ΔE_0 for the Pt-Pt and Pt-M coordination shells in the Pt alloys at 0.84 V are listed in Table VII. Even though analysis of the EXAFS failed to reveal any oxygenated species chemisorbed to the Pt surface on the PtMn/C alloy the XANES data indicated some adsorption of OH, albeit to a lesser extent than on the Pt/C electrocatalyst (Table III). Further, there is no change in the bond distance for all electrocatalysts when the potential is increased from 0.54 to 0.84 V (Tables III-VII). With the exception of Pt/C there is no change in the Pt-Pt coordination numbers on going to 0.84 V (Tables III and V).

Correlations of results of electrochemical and XAS studies.—Our main objective here is to see if there are any cor-

Downloaded 09 Mar 2011 to 129.10.187.55. Redistribution subject to ECS license or copyright; see http://www.ecsdl.org/terms_use.jsp

Table V. Results of *in situ* EXAFS analysis at the Pt L_3 edge for supported Pt/C electrocatalyst at 0.54 and 0.84 V *vs.* RHE.

Coordination shell	EXAFS parameter at 0.54 V *vs.* RHE				EXAFS parameter at 0.84 V *vs.* RHE			
	N	R (Å)	$\Delta\sigma^2$	ΔE_o	N	R (Å)	$\Delta\sigma^2$	ΔE_o
Pt-Pt	8.66	2.773	0.0044	−0.88	6.73	2.773	0.0048	−0.20
Pt-O					1.69	2.037	0.0042	2.48

Errors were typically 1 to 8% (N) and 0.005 to 0.01 Å (R) for single-shell fits.

Table VI. Results of *in situ* EXAFS analysis at the Pt L_3 edge for supported Pt alloy electrocatalysts at 0.54 V *vs.* RHE.

Coordination shell	EXAFS parameter	Alloying element				
		Mn	Cr	Fe	Co	Ni
Pt-Pt	N	7.52	8.53	6.71	6.94	9.12
	R	2.762	2.713	2.701	2.684	2.683
	$\Delta\sigma^2$	0.00574	0.00663	0.00341	0.00575	0.00722
	ΔE_o	1.04	5.20	9.45	5.48	7.55
Pt-M	N	2.75	2.78	2.98	2.48	2.72
	R	2.682	2.690	2.640	2.631	2.613
	$\Delta\sigma^2$	0.00226	0.00392	0.00654	0.00613	0.01141
	ΔE_o	−8.11	−7.58	−6.51	−8.37	−9.12

Errors were typically 5 to 14% (N) and 0.007 to 0.012 Å (R) for two-shell fits.

Table VII. Results of *in situ* EXAFS analysis at the Pt L_3 edge for supported Pt alloy electrocatalysts at 0.84 V *vs.* RHE.

Coordination shell	EXAFS parameter	Alloying element				
		Mn	Cr	Fe	Co	Ni
Pt-Pt	N	8.31	8.82	6.40	7.62	9.45
	R	2.762	2.713	2.711	2.684	2.683
	$\Delta\sigma^2$	0.00624	0.00693	0.00392	0.00624	0.00773
	ΔE_o	0.92	5.92	3.17	5.39	7.59
Pt-M	N	2.86	2.89	2.43	2.34	3.34
	R	2.681	2.700	2.652	2.631	2.583
	$\Delta\sigma^2$	0.00291	0.00376	0.00276	0.00593	0.01432
	ΔE_o	−7.38	−8.79	−10.06	−8.45	−6.97

Errors were typically 5 to 14% (N) and 0.007 to 0.012 Å (R) for two-shell fits.

relations between the electrode kinetic parameters and the electronic and geometric characteristics of the Pt and Pt alloy electrocatalyst. The Tafel slope in the region of potential for fuel cell operation does not show any dependence on change in the electronic and structural parameters as a result of alloying Pt with the first-row transition elements (see results in Tables I and III). However, the electrocatalytic activities show a dependence, as seen from the i_o and i_{900mV} values in Table I and the Pt 5 d-orbital vacancy per atom $(h_J)_{t,s}$ and Pt-Pt (R) values in Table III. The current density at 900 mV in the fuel cell is close to the open-circuit potential. At this potential the only contribution to the overpotential is the activation overpotential for the oxygen electrode. For an illustration of the role of electronic and structural properties in the electrocatalysis of oxygen reduction on Pt and Pt alloys, plots were made of log i_{900mV} *vs.* $(h_J)_{t,s}$ and Pt-Pt (R) bond distances (Fig. 14). Volcano type behavior for oxygen reduction in these plots is similar to that observed earlier by Appleby[45] in phosphoric acid. The primary difference being that the earlier studies involved the correlation of the electrochemical performance with *ex situ* measurements (XRD) for the Pt-Pt bond distance[1] and calculated value of percentage d-band character,[45] whereas in this study the volcano plots are derived from an actual *in situ* correlation involving both the Pt-Pt distances and the d-band electronic properties. The theoretical basis of volcano behavior[45] indicates that at a fixed p_{O_2} and $\{H^+\}$, the rate (log i) should illustrate ascending and descending linear functions of ΔG_{OH} with the maximum being at $\Delta G_{OH} = 0$. This approach therefore implies that the Pt/C, PtMn/C electrocatalysts have high overpotentials with $\Delta G_{OH} < 0$ followed by PtCr/C with $\Delta G_{OH} \sim 0$ and PtFe/C, PtNi/C, PtCo/C electrocatalysts again having high overpotentials with $\Delta G_{OH} > 0$.

From the results shown above, there are principally three interrelated factors controlling the electrocatalysis of oxygen reduction reaction. These are (*i*) the vacancies of the Pt 5 d-orbitals, (*ii*) the Pt-Pt bond distance, and (*iii*) the adsorption characteristics of the oxygenated species from the electrolyte solution. The interplay of a redox type process was, however, ruled out on the basis that position of the K-edge XANES of alloying elements was unaffected as a result of potential transition from 0.54 to 0.84 V (Fig. 15-19). A change in the oxidation state, expected as a result of a redox type process is therefore absent. This is illustrated in the PtNi/C alloy electrocatalyst, where there is no change in the Ni K-edge XANES in the potential region of 0.0 to 1.14 V *vs.* RHE (Fig. 15). It also indicates that there is no corrosion of Ni at positive potentials. In the case of PtCr/C electrocatalyst, there was still much residual Cr oxide, even after the KOH treatment, which yielded a yellow chromate solution. This could be seen in both the Cr EXAFS, which exhibited a Cr-O peak and in the XANES spectra (Fig. 16). This obscures the interpretation of the Cr data. However, there was no observable edge shift or increase in the Cr white line, as evident from the spectra at 0.54 and 0.84 V. In the Mn and Fe alloys, there was some increase in the white line at 0.84 V (as compared with that at 0.54 V) without any change in the edge position. This may indicate adsorption of oxygen species or the onset of corrosion (Fig. 17-18). At 1.14 V, there was a slight increase in the Co XANES white line (Fig. 19), indicating the onset

Downloaded 09 Mar 2011 to 129.10.187.55. Redistribution subject to ECS license or copyright; see http://www.ecsdl.org/terms_use.jsp

of corrosion. In all cases there was no evidence of a redox process in the oxygen reduction potential region.

It is evident that the partly filled d-orbitals and bond distances of the transition elements play an important role in the oxygen reduction electrocatalysis. The first reports of this fact[45,47] were based on correlation of calculated values of the percentage d-orbital vacancies (using Pauling's equation[48]) and bond distances obtained from XRD analysis for the transition elements such as Au, Pt, Pd, Ir, Rh, Ru, Os, etc., with the electrochemical performance characteristics which exhibited the volcano type behavior. Results from this study support these earlier correlations and provide the framework for altering the electronic and geometric parameters of catalytically active surfaces by alloying Pt with first-row transition elements. Further fine-tuning of the ORR electrocatalysis may be possible via formation of ternary alloys.[49]

Conclusions

From the results presented above it is evident that ORR electrocatalysis depends primarily on the interplay of electronic and geometric parameters, which in turn controls the adsorption of OH species from the electrolyte at potentials above 0.80 V. The role of electronic factors in electrocatalysis can be better appreciated by considering the changes in the work function of the Pt atom due to alloying. The work function can be directly related to the metal (Pt) adsorbate bond strength ($D_{M\text{-}Ads}$). The metal-adsorbate bond strength in turn can be related to the electronegativity of the catalytically active metal surface via Pauling's equation, as used by Eley[50]

$$D_{M\text{-}Ads} = 1/2(D_{M\text{-}M} + D_{Ads\text{-}Ads}) + 23.06(X_M - X_{Ads})^2 \quad [6]$$

where the $D_{M\text{-}M}$ and $D_{Ads\text{-}Ads}$ are the metal-metal and adsorbate-adsorbate bond strength and the X_M and X_{Ads} are the electronegativities of the metal and the adsorbate. Since X_{Ads} is the only variable in the above equation, it implies that any change in the electronegativity of Pt results in changes in the Pt-OH bond strength. This could partly ex-

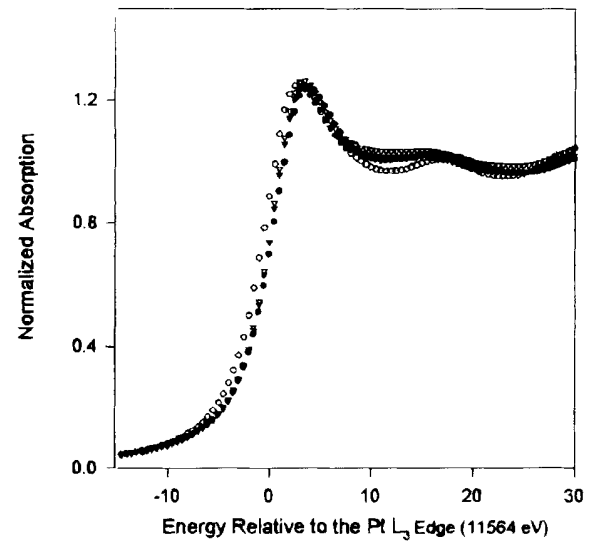

Fig. 9. XANES spectra at the Pt L_3 edge for (a) PtCr/C (●), PtMn/C (▽), PtFe/C (▼) and (b) Pt/C (△), PtCo/C (□), PtNi/C (■) relative to a Pt reference foil (○) at 0.84 V in 1*M* $HClO_4$.

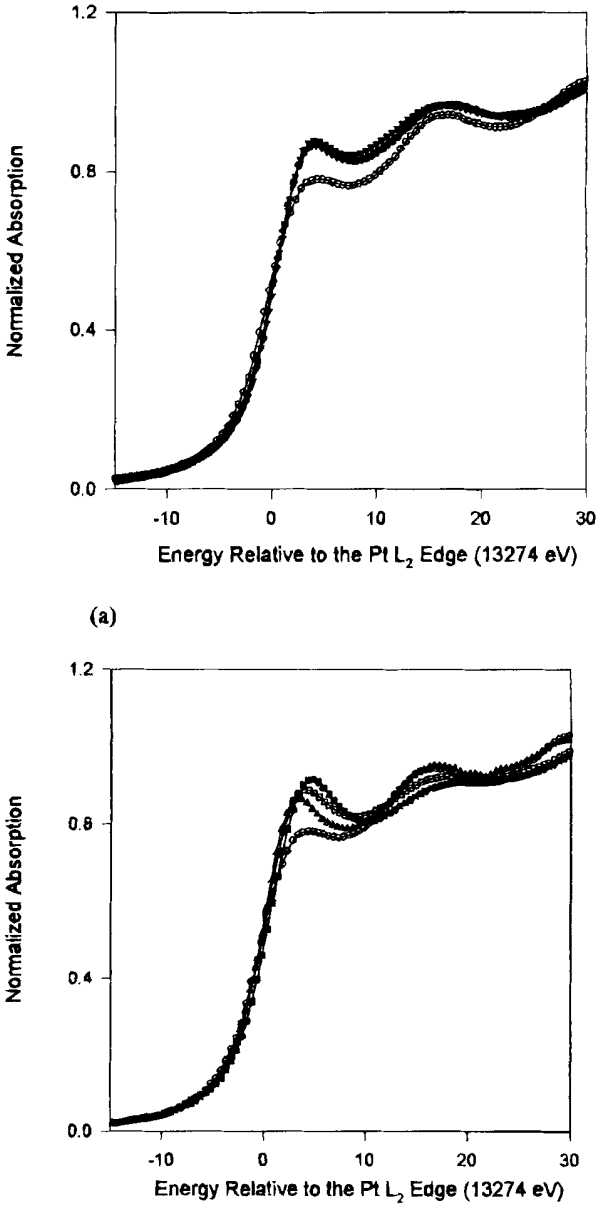

Fig. 10. XANES spectra at the Pt L_2 edge for (a) PtCr/C (●), PtMn/C (▽), PtFe/C (▼) and (b) Pt/C (△), PtCo/C (□), PtNi/C (■) relative to a Pt reference foil (○) at 0.84 V in 1*M* $HClO_4$.

Downloaded 09 Mar 2011 to 129.10.187.55. Redistribution subject to ECS license or copyright; see http://www.ecsdl.org/terms_use.jsp

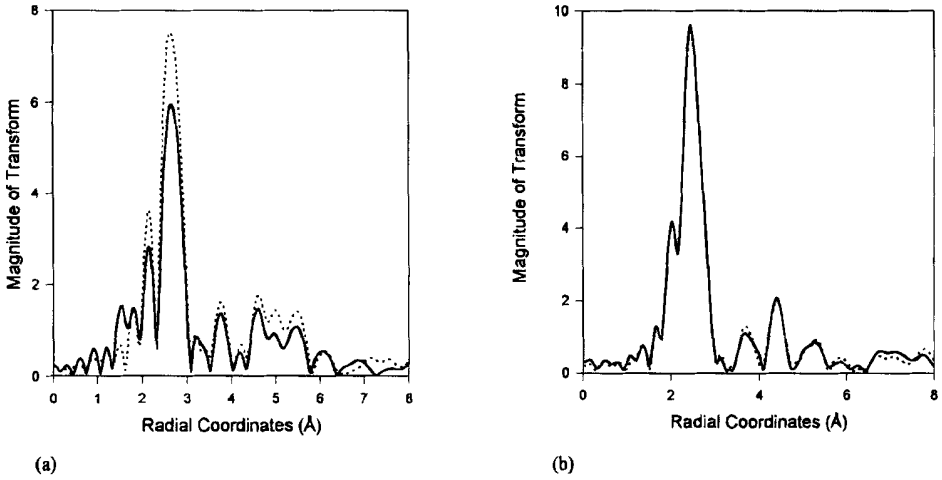

Fig. 11. Forward Fourier transform (k^3 weighted) at potentials of 0.54 {···} and 0.84 V {—} for (a) Pt/C and (b) PtCr/C electrocatalyst (Δk values in Table IV).

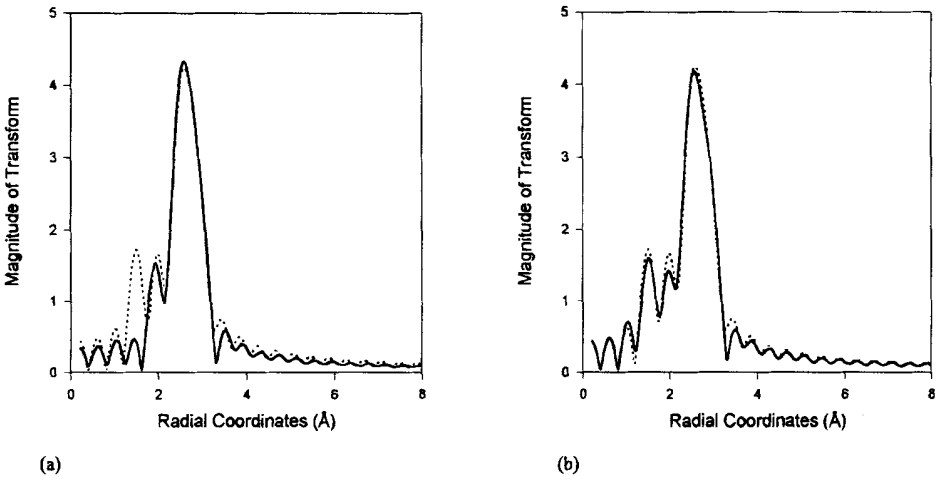

Fig. 12. Fits in r-space for the EXAFS data of Pt/C electrocatalyst at 0.84 V; (a) a single Pt-Pt shell and (b) a two-shell fit with Pt-Pt and Pt-O coordination, (···) experimental data, (—) fit, k^3 weighted.

plain the lack of affinity for OH chemisorption on Pt surface in the alloys at potential above 0.80 V.

Sensitivity of the ORR activity to bond distances has been independently[1,45,51] established. As shown by Chen and Gerwith,[51] underpotential deposited (UPD) layers of Bi on Au cause variations in bond distances and hence the bond strength of the intermediates during H_2O_2 reduction, thereby effecting the activation energy and reaction order for the reduction step. Similarly, the sensitivity of the Pt-Pt coordination numbers toward the ORR has been pointed out previously[52] based on investigations of supported Pt electrocatalysts. According to this investigation, higher ORR electrocatalytic activity may be caused by higher concentration of crystallites with low Pt-Pt coordination numbers.

The following conclusions can be drawn from the results of the present work.

1. The kinetic parameters for ORR electrocatalysis obtained at 95°C and 5 atm pressure in PEMFC indicate a two- to threefold enhancement for the binary Pt alloys as compared to the base line performance of the Pt/C electrocatalyst (the Pt loading in all the electrodes remaining constant at 0.3 mg cm^{-2}). This was observed for the exchange current density, current density at 900 mV, and potential at 10 mA cm^{-2}, based on geometric and true surface areas (electrochemically active surface area of Pt). Among the binary Pt alloys, the highest performance was shown by the PtCr/C alloy electrocatalyst.

2. The XRD studies reveal that alloys of Pt with base transition elements of group VIB to VIIB (Cr to Ni) primarily possess the Pt_3M phase with the LI_2 type fcc lattice structure and a secondary phase (only small contributions of 2 to 9% from this phase) of the PtM type with LI_o type tetragonal lattice structure. This formation of an intermetallic alloy therefore causes a contraction in the Pt-Pt bond distance. In addition, the sizes of the alloy particles exhibit a 1.6 to twofold increase over that on the Pt/C electrocatalyst.

3. The *in situ* XANES investigation at a potential in the double-layer region (0.54 V) reveals that the d-band vacancies of the Pt 5 d-orbital (with the exception of PtMn/C) are higher for the alloys than for Pt/C electrocatalyst. As expected, the change in the d-orbital vacancies follows the same trend as the electronegativity variations of the alloying element. EXAFS investigations at a potential in the double-layer region show lattice contractions for the Pt-Pt bond distances in the alloys which are in agreement with those obtained from the XRD investigations. At a potential of 0.54 V in $HClO_4$ there was no indication of any chemisorbed oxygenated species on any of the electrocatalysts (Pt and Pt alloy electrocatalyst). The Pt-Pt bond distance and the Pt 5 d-band vacancies in the Pt alloys exhibited a smooth and inverse relationship indicating the close interplay of the geometric and electronic factors.

4. Comparison of the *in situ* XANES and EXAFS investigation at 0.54 and 0.84 V revealed that the Pt/C electrocatalyst, in contrast to Pt alloys (with the exception of PtMn/C alloy to some extent), shows a significant increase in the d-band vacancy as a result of such a potential transition. This could be accounted for by the lack of affinity of OH chemisorption on the Pt in Pt alloys, unlike that on the Pt/C electrocatalyst. This fact is also evident by comparison of the *in situ* EXAFS results at the two potentials. The principal factors responsible for this behavior are the changes in the d-band vacancy, which affects the electronegativities/electron affinities of the Pt atom in the al-

Downloaded 09 Mar 2011 to 129.10.187.55. Redistribution subject to ECS license or copyright; see http://www.ecsdl.org/terms_use.jsp

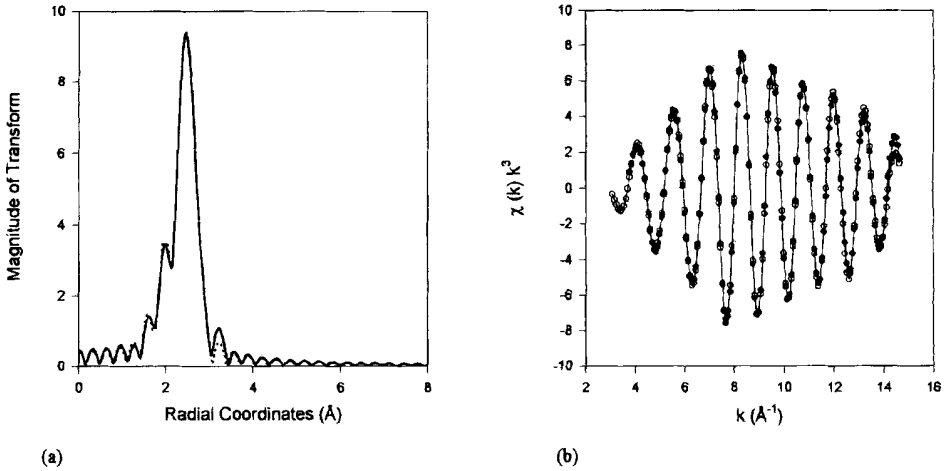

Fig. 13. A two-shell fit (Pt-Pt and Pt-Cr) for the EXAFS of PtCr/C sample at 0.84 V in (a) *r*-space and (b) *k*-space. The fits are k^3 weighted with the sample data denoted by [(···) in *r* and (○) in *k* space] and the fit data by [(—) in *r* and (●) in *k* space].

loys and the presence of the alloying element with a greater affinity to adsorb any oxygenated species. Thus, there are more surface sites for adsorption of molecular dioxygen on the Pt surface in the alloys than on Pt/C electrocatalyst. The Pt-Pt bond distances and the coordination numbers obtained by the *in situ* EXAFS analysis at the two potentials (0.54 and 0.84 V), do not show any significant variations for the alloys; in contrast Pt/C electrocatalyst exhibits variation in the Pt-Pt coordination numbers (the bond distances remaining the same) at the two potentials due to the adsorption of OH species from the electrolyte solution at the higher potential.

5. Plot of electrocatalytic activity (i_{900mV}) *vs.* the electronic (Pt *d*-band vacancies per atom) and geometric parameters (Pt-Pt bond distances) exhibit a volcano type behavior. PtCr/C lies at the top of the curve, revealing the fact that, among the electrocatalysts investigated, it has the best combination of both the Pt *d*-band vacancies as well as the Pt-Pt bond distance. The volcano type relationship implies that $\Delta G_{OH(Ads)}$ is close to zero for the PtCr/C alloy and greater than zero for the PtFe/C, PtCo/C, and PtNi/C alloys. PtMn/C and Pt/C lie on the ascending part of the volcano curve implying $\Delta G_{OH(Ads)} < 0$ as a result of which they are expected to show OH adsorption in the oxygen reduction region. The Pt atom in the Pt/Mn alloy, however, did not indicate the presence of any oxygenated species in the *in situ* EXAFS analysis, which is primarily due to the fact that the change in the *d*-band vacancy was not as significant at 0.84 V as compared to the Pt/C electrocatalyst. However, the presence of oxygenated species at higher potentials can be expected assuming a Temkin type isotherm for OH adsorption in this part of the volcano curve.

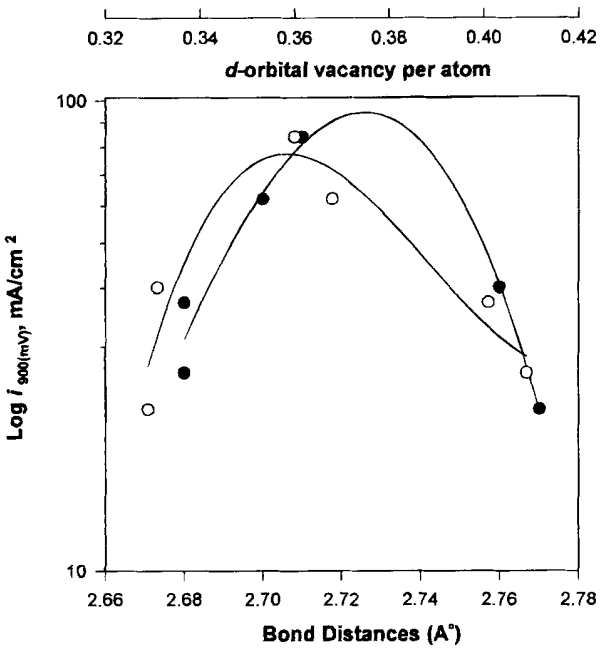

Fig. 14. Correlation of oxygen electrode performance (Log $i_{900\,mV}$, mA cm^{-2}) of Pt and Pt alloy electrocatalysts in PEMFC with Pt-Pt bond distance {●} and the *d*-orbital vacancy of Pt {○} obtained from *in situ* XAS.

Acknowledgment

The authors gratefully acknowledge the support of the National Aeronautic and Space Administration-Johnson Space Center under the auspices of the Regional University Grant Program (Grant No. NAG 9-533), Center for Energy and Mineral Resources, Texas A&M University, and the U.S. Department of Energy, Division of Material Science, Brookhaven National Laboratory (Contract No. DEA-CO2-76CH00016) for its role in the development and operation of the National Synchroton light Source (NSLS). This work carried out by one of us (S. M.) was in partial fulfillment of the requirements for the Ph.D. degree in Chemistry at Texas A&M University. The help of NIST personnel at the Beam Line X23A2, in particular Joe Woicik and John Kirkland, is gratefully acknowledged. The authors also

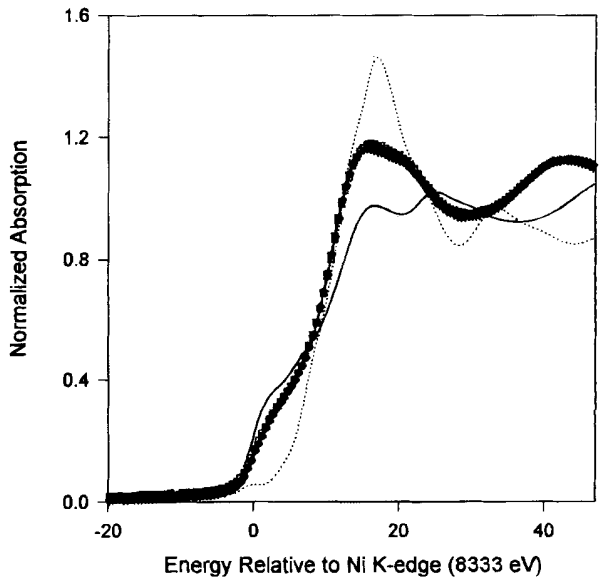

Fig. 15. Ni K-edge XANES for the PtNi/C electrocatalyst at 0.54 (▽), 0.84 V (◇), and 1.14 V (□) relative to NiO (···) and Ni foil standard (—).

Downloaded 09 Mar 2011 to 129.10.187.55. Redistribution subject to ECS license or copyright; see http://www.ecsdl.org/terms_use.jsp

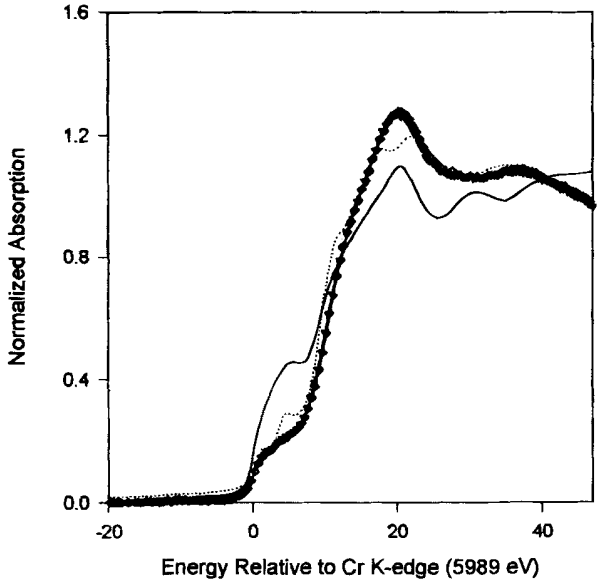

Fig. 16. Cr K-edge XANES for the PtCr/C electrocatalyst at 0.54 (▽) and 0.84 V (◇) relative to Cr_2O_3 (···) and Cr foil standard (—).

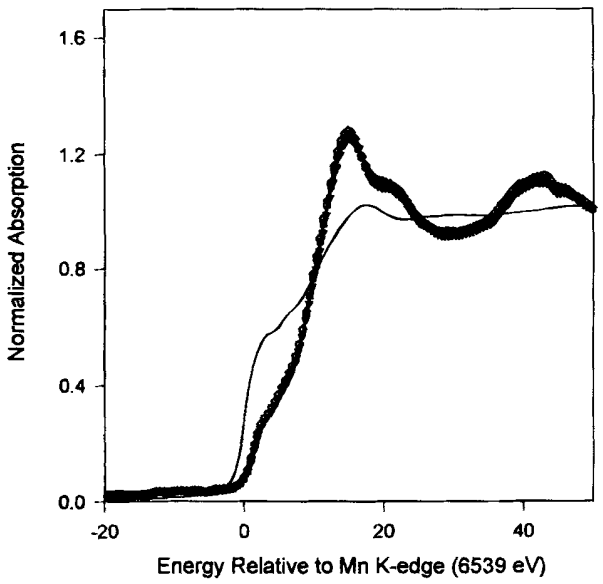

Fig. 17. Mn K-edge XANES for the PtMn/C electrocatalyst at 0.54 (▽) and 0.84 V (◇) relative to an Mn foil standard (—).

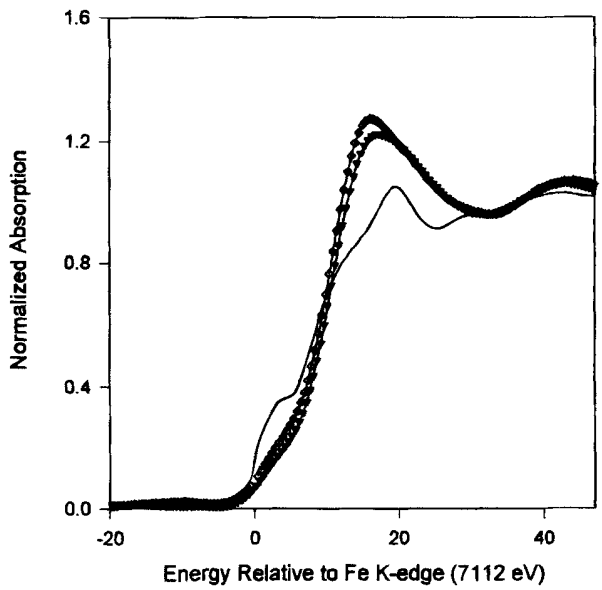

Fig. 18. Fe K-edge XANES for the PtFe/C electrocatalyst at 0.54 (▽) and 0.84 V (◇) relative to an Fe foil standard (—).

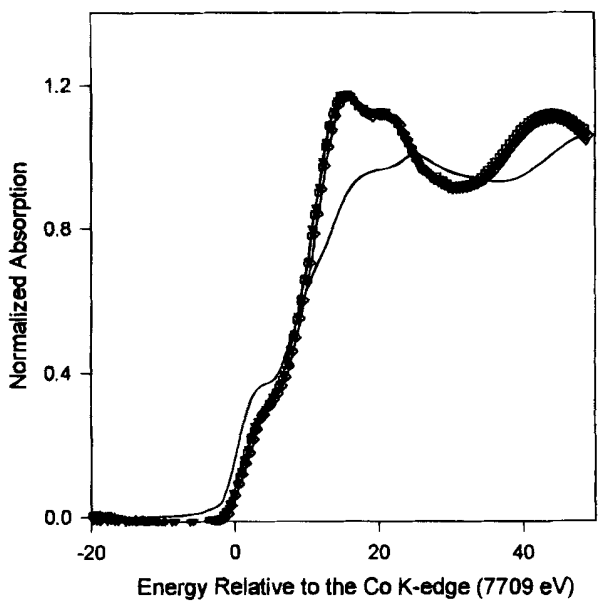

Fig. 19. Co K-edge XANES for the PtCo/C electrocatalyst at 0.54 (▽), 0.84 (◇), and 1.14 V (□) relative to a Co foil standard (—).

wish to acknowledge the helpful suggestions and discussions with A. Cesar Ferreira, CESHR, Texas A&M University, Kaumudi Pandya, Applied Science Division, Brookhaven National Laboratory, and Lindsay Keck of Johnson-Matthey Corp., who also supplied the electrocatalysts. The support of the Office of Transportation Technologies, Electric and Hybrid Vehicles Division of D.O.E. is gratefully acknowledged.

Manuscript submitted Dec. 20, 1993; revised manuscript received Dec. 20, 1994. This was in part Paper 1749 presented at the Honolulu, HI, Meeting of the Society, May 16-21, 1993.

Brookhaven National Laboratory assisted in meeting the publication costs of this article.

REFERENCES

1. V. M. Jalan and E. J. Taylor, *This Journal*, **130**, 2299 (1983).
2. J. T. Glass, G. L. Cahen, and G. E. Stoner, *ibid.*, **134**, 58 (1987).
3. M. T. Paffett, J. G. Beery, and S. Gottesfeld, *ibid.*, **135**, 1431 (1988).
4. B. C. Beard and P. N. Ross, Jr., *ibid.*, **130**, 3368 (1990).
5. A. J. Appleby, *Catal. Rev.*, **4**, 221 (1970).
6. J. A. S. Bett, in *Proceedings of Symposium on Structural Effects in Electrocatalysis and Oxygen Electrochemistry*, D. Scherson, D. Tryk, M. Deroux, and X. Xing, Editors, PV 92-11, P. 573, The Electrochemical Society Proceedings Series, Pennington, NJ (1992).
7. S. Mukerjee and S. Srinivasan, *J. Electroanal. Chem.*, **357**, 201 (1993).
8. R. Parsons and T. Vandernoot, *ibid.*, **257**, 9 (1988).
9. H. D. Abruna, *Electrochemical Interface: Modern Techniques for In-Situ Interface Characterization*, VCH Publishers, Inc., New York (1991).
10. E. A. Ticianelli, C. R. Derouin, and S. Srinivasan, *J. Electroanal. Chem.*, **251**, 275 (1988).
11. S. Srinivasan, E. A. Ticianelli, C. R. Derouin, and A. Redondo, *J. Power Sources*, **22**, 359 (1988).
12. A. C. Ferreira, S. Srinivasan, and A. J. Appleby, Abstract 7, p. 11, The Electrochemical Society Extended

Downloaded 09 Mar 2011 to 129.10.187.55. Redistribution subject to ECS license or copyright; see http://www.ecsdl.org/terms_use.jsp

Abstracts, Vol. 92-1, St. Louis, MO, May 17-22 (1992).
13. S. Mukerjee, S. Srinivasan, and A. J. Appleby, *Electrochim. Acta.*, **38,** 1661 (1993).
14. A. Parthasarathy, S. Srinivasan, and A. J. Appleby, *J. Electroanal. Chem.*, **339,** 101 (1992).
15. J. A. Golovchenko, R. A. Levesque, and P. L. Cowan, *Rev. Sci. Instrum.*, **52,** 509 (1981).
16. P. L. Cowan, J. B. Hastings, T. Jach, and J. P. Kirkland, *Nucl. Instrum. Mech.*, **208,** 349 (1983).
17. J. McBreen, W. E. O'Grady, K. I. Pandya, R. W. Hoffman, and D. E. Sayers, *Langmuir,* **3,** 428 (1987).
18. T. Swanson, *Natl. Bur. Stand. (U.S.), Circ.,* **1,31,** 539 (1953).
19. J. Baglin, *This Journal,* **125,** 1854 (1978).
20. E. Raub and W. Mahler, *Z. Mettalkd.*, **46,** 210 (1955).
21. A. Kussman and G. G. V. Rittberg, *ibid.*, **41,** 470 (1950).
22. A. H. Geisler and D. L. Martin, *J. Appl. Phys.*, **23,** 375 (1952).
23. C. Leroux, C. Cadeville, V. Pierron-Bohnes, G. Inden, and F. Hinz, *Phys. Rev. F.,* **18,** 2033 (1988).
24. H. Klug and L. Alexander, *X-Ray Diffraction Procedures,* p. 491, Wiley, New York (1962).
25. L. V. Azaroff, *Elements of X-Ray Crystallography,* p. 556, McGraw Hill, New York (1968).
26. *Valence Fluctuations in Solids,* L. M. Falicov, W. Hanke, and M. P. Maple, Editors, North-Holland Pub., Amsterdam (1981).
27. M. Brown, R. E. Peierls, and D. E. Stern, *Phys. Rev. B.*, **15,** 738 (1977).
28. L. F. Matheiss and R. E. Dietz, *ibid.*, **22,** 1663 (1980).
29. A. N. Mansour, Ph.D Thesis, University of North Carolina, Raleigh, NC (1983).
30. A. N. Mansour, J. W. Cook, Jr., and D. E. Sayers, *J. Chem. Phys.*, **88,** 2330 (1984).
31. A. N. Mansour, J. W. Cook, Jr., D. E. Sayers, R. J. Emrich, and J. R. Katzer, *J. Catal.*, **89,** 464 (1984).
32. M. G. Samant and M. Boudart, *J. Phys. Chem.*, **95,** 4070 (1991).
33. D. E. Sayers and D. A. Bunker, *X-Ray Absorption: Principles, Applications, Techniques of EXAFS, SEXAFS and XANES,* D. C. Koningsberger and R. Prins, Editors, John Wiley & Sons, New York (1988).
34. J. Wong, F. W. Lytle, R. P. Messner, and D. H. Maylotte, *Phys. Rev. B.*, **30,** 5596 (1984).
35. W. H. McMaster, N. Kerr Del Grande, J. H. Mallett, and J. H. Hubbel, *Compilation of X-Ray Cross Sections,* National Technical Information Service, Springfield, VA (1969).
36. J. B. A. D. van Zon, D. C. Koningsberger, H. F. J. vant'Blik, and D. E. Sayers, *J. Chem. Phys.*, **82,** 5742 (1985).
37. F. B. M. Duivenvoorden, D. C. Koningsberger, Y. S. Oh, and B. C. Gates, *J. Am. Chem. Soc.*, **108,** 6254 (1986).
38. K. I. Pandya, W. E. O'Grady, D. A. Corrigan, J. McBreen, and R. W. Hoffman, *J. Phys. Chem.*, **94,** 21 (1990).
39. K. I. Pandya, R. W. Hoffman, J. McBreen, and W. E. O'Grady, *This Journal,* **137,** 383 (1990).
40. G. Tourillon, H. Dexpert, and P. Lagarde, *This Journal,* **134,** 327 (1987).
41. P. H. Citrin, P. Eisenberger, and B. M. Kincaid, *Phys. Rev. Lett.*, **36,** 1346 (1976).
42. J. J. Rehr, J. Mustre de Leon, S. I. Zabinski, and R. C. Albers, *J. Am. Chem. Soc.*, **113,** 5135 (1991).
43. B. K. Teo, *EXAFS: Basic Principles and Data Analysis,* Inorganic Concepts 9, p. 132, Springer Verlag, Berlin (1986).
44. M. E. Herron, S. E. Doyle, S. Pizzini, K. J. Roberts, J. Robinson, G. Hards, and F. C. Walsh, *J. Electroanal. Chem.*, **324,** 243 (1992).
45. A. J. Appleby, *Catal. Rev.*, **4,** 221 (1970).
46. A. J. Appleby, *J. Electroanal. Chem.*, **357,** 117 (1993).
47. M. L. B. Rao, A. Damjanovic, and J. O'M. Bockris, *J. Phys. Chem.*, **67,** 2508 (1963).
48. L. Pauling, *Proc. R. Soc. London, Ser. A,* **196,** 343 (1943).
49. F. J. Luczak and D. A. Landsman, U.S. Pat. 4,711,829 (1987).
50. D. D. Eley, *J. Phys. Colloid Chem.*, **55,** 1017 (1951).
51. C. Chen and A. A. Gerwith, *J. Am. Chem. Soc.*, **114,** 5440 (1992).
52. M. Peuckert, T. Yoneda, R. A. Dalla Beta, and M. Boudart, *This Journal,* **133,** 944 (1988).

Downloaded 09 Mar 2011 to 129.10.187.55. Redistribution subject to ECS license or copyright; see http://www.ecsdl.org/terms_use.jsp